

Cavity-Enhanced Optical Lattices for Scaling Neutral Atom Quantum Technologies to Higher Qubit Numbers


A. J. Park,^{1,2} J. Trautmann^{1,2}, N. Šantić^{1,2,3}, V. Klüsener,^{1,2} A. Heinz,^{1,2,†} I. Bloch,^{1,2,4} and S. Blatt^{1,2,*}

¹Max-Planck-Institut für Quantenoptik, Hans-Kopfermann-Straße 1, Garching 85748, Germany

²Munich Center for Quantum Science and Technology, München 80799, Germany

³Institute of Physics, Bijenička cesta 46, Zagreb 10000, Croatia

⁴Fakultät für Physik, Ludwig-Maximilians-Universität München, München 80799, Germany

 (Received 15 October 2021; revised 20 February 2022; accepted 11 July 2022; published 28 July 2022)

We demonstrate a cavity-based solution to scale up experiments with ultracold atoms in optical lattices by an order of magnitude over state-of-the-art free-space lattices. Our two-dimensional (2D) optical lattices are created by power-enhancement cavities with large mode waists of $489(8) \mu\text{m}$ and allow us to trap ultracold strontium atoms at a lattice depth of $60 \mu\text{K}$ by using only 80 mW of input light per cavity axis. We characterize these lattices using high-resolution clock spectroscopy and resolve carrier transitions between different vibrational levels. With these spectral features, we locally measure the lattice potential envelope and the sample temperature with a spatial resolution limited only by the optical resolution of the imaging system. The measured ground-band and trap lifetimes are $18(3) \text{ s}$ and $59(2) \text{ s}$, respectively, and the lattice frequency (depth) is long-term stable on the megahertz (0.1%) level. Our results show that large, deep, and stable 2D cavity-enhanced lattices can be created at any wavelength and can significantly increase the qubit number for neutral-atom-based quantum simulators, quantum computers, sensors, and optical-lattice clocks.

DOI: [10.1103/PRXQuantum.3.030314](https://doi.org/10.1103/PRXQuantum.3.030314)

I. INTRODUCTION

Far-off-resonant optical dipole traps formed by laser light are a foundational technology for modern quantum science [1,2] and are used in quantum simulators [3], quantum computers [4–7], optical clocks [8], and matter-wave interferometers [9]. When such traps make use of interference between multiple laser beams, they form optical lattices consisting of arrays of nearly identical microtraps that can hold ultracold atoms. The energy barrier between the microtraps can be tuned by changing the laser intensity.

Lowering the barriers between the traps lets the atoms tunnel between lattice sites and interact, which is the basis of analog quantum simulations [10] of foundational quantum many-body models. These models are important in

condensed-matter physics [3,11], quantum optics [12–14], quantum chemistry [15], and high-energy physics [16,17].

Raising the barriers between the traps prevents any quantum tunneling or thermally activated hopping of atoms between the traps, creating an array of independent and identical quantum systems. This parallelism allows simultaneous interrogation and averaging of the signal derived from many identical systems, which is the basis of optical-lattice clocks [18,19].

The system sizes that can be simulated on quantum simulators and the precision of optical-lattice clocks are both limited by the number of identical lattice sites that can be used. Since optical lattices are created by laser beams, the lattice sites are no longer identical on length scales that are comparable to the finite transverse extent of the beams because the lattice potential depth varies. This inhomogeneity limits scaling atomic quantum technologies to higher numbers of atoms or qubits.

In analog quantum simulators, the depth variation in the optical-lattice potential leads to a spatial variation of the tunneling rate, the interaction parameters, and the chemical potential. Therefore, descriptions of such quantum systems must rely on local-density approximations [20] and take edge effects into account. Analog quantum simulations are often initialized in a low-entropy Mott-insulating

*sebastian.blatt@mpq.mpg.de

†Current address: TOPTICA Photonics, Lochhamer Schlag 19, 82166 Gräfelfing, Germany.

Published by the American Physical Society under the terms of the [Creative Commons Attribution 4.0 International](https://creativecommons.org/licenses/by/4.0/) license. Further distribution of this work must maintain attribution to the author(s) and the published article's title, journal citation, and DOI.

state, where each lattice site is occupied by a single atom [20]. The lattice inhomogeneity limits the size and fidelity of this Mott-insulating state, which in turn restricts the size and fidelity of the analog quantum simulation.

Scaling up quantum resources will also improve the stability of state-of-the-art optical-lattice clocks. The fundamental limit to clock stability is the quantum projection noise, which scales $\propto 1/\sqrt{N}$, where N is the number of concurrently interrogated atoms. In one-dimensional (1D) optical-lattice clocks (the most common type), increasing the atom number leads to interaction-induced frequency shifts [21–23], which lower the accuracy of the clock. These shifts can be reduced by using two-dimensional (2D) [24] or three-dimensional (3D) lattices [25,26], in which case N is limited by the mode area or mode volume of the optical lattices, respectively. Here, the mode area (volume) refers to the overlap area (volume) of the two (three) orthogonal beams that create the lattices, an area directly proportional to the number of usable lattice sites, and thus N .

For these reasons, solutions to the lattice-inhomogeneity problem have been long sought after. Toward this goal, methods to improve the homogeneity have been investigated, such as increasing the lattice beam waist [19,27], the addition of compensating laser beams [28–30], and the projection of box potentials [31,32]. Out of these methods, increasing the lattice beam waist provides the most fundamental improvement, because it is compatible with additional potential-shaping methods. Moreover, it also provides the most significant improvement: linearly increasing the beam waist quadratically increases the mode area of 2D optical lattices. However, increasing the beam waist is limited by the available laser power. A standard solution to limited laser power is to enhance it in an optical cavity and many research groups have created 1D optical lattices for different purposes [19,27,33–38]. However, work on 2D [39,40] or 3D cavity lattices [25] is much more scarce, because significant technical challenges must be overcome to ensure stable trapping.

First, the cavity beams must be spatially overlapped precisely to generate optical lattices with a large mode area (volume) in 2D (3D). Obtaining and preserving a good overlap requires long-term mechanical and thermal stability of the whole cavity assembly. These stability requirements become much harder to fulfill for an increased beam waist, because the mode overlap is sensitive to angular misalignments and this sensitivity scales with the fourth power of the mode waist [41,42]. Second, cavity-enhanced lattices cause increased atomic heating compared to free-space lattices by converting laser phase noise and mechanical vibrations into lattice-intensity noise. Therefore, a viable cavity setup for increasing the size of optical lattices must support a large cavity-mode size, a high degree of mechanical stability, and a long atomic lifetime.

In this work, we demonstrate the first stable 2D cavity-enhanced optical lattices with a mode area close to 1 mm^2 that can trap neutral atoms in both high- and low-intensity lattice regimes, enabling experiments with both isolated and tunneling atoms. Our cavity assembly contains two independent perpendicular optical cavities that cross at right angles, creating a square lattice with a lattice spacing of $\lambda/2$, where λ is the wavelength of the lattice light. Our assembly is monolithic, as shown in Fig. 1(a), ensuring a high degree of mechanical and thermal stability. By precisely optical contacting cavity mirrors to an ultra-low-expansion glass spacer [42], we achieve a stable and near-perfect overlap of two orthogonal modes for the first time. Our new cavity-enhanced 2D lattice setup can be adapted to any wavelength of interest, even those for which the available laser power is limited, and our cavity is coated for multiple wavelengths relevant for experiments with ultracold strontium atoms. We demonstrate the advantage of this capability by creating our lattices at an unconventional wavelength of 914.3 nm and show an improvement of more than an order of magnitude in system size over free-space setups based on the same lasers.

We briefly discuss the design of the cavity assembly and its integration into our vacuum system in Sec. II. Then, we characterize the 2D cavity lattices by loading strontium

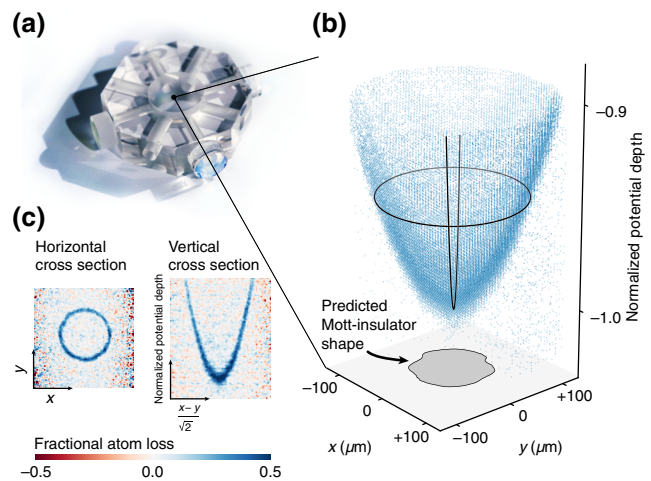


FIG. 1. (a) A photograph of the monolithic cavity assembly. The two-dimensional (2D) optical lattice is formed at the intersection of the optical axes of both cavities. (b) A three-dimensional scatter plot of the measured potential envelope of the optical lattice. The potential is reconstructed by vertically stacking images (with spatial coordinates x and y) that represent the fractional atom loss after clock-laser excitation at a given clock-laser detuning (see Sec. III). The reconstructed envelope confirms that each cavity supports a fundamental TEM_{00} mode with a $1/e^2$ waist of $489(8) \mu\text{m}$ at 914.3 nm. A Mott insulator of strontium atoms created in an optical lattice with this potential envelope is expected to form in the shaded area, which has a diameter of approximately $125 \mu\text{m}$. (c) Cross sections through the image stack corresponding to horizontal and vertical lines drawn in (b). The color bar indicates the fractional loss of atoms.

atoms and performing clock spectroscopy at a wavelength where the differential light shift of the clock states is large. We observe spatially dependent clock excitation that exhibits carrier and sideband transitions. The high spectral resolution lets us observe vibrational-mode-specific carrier transitions for the first time. These new spectral features provide access to the potential and population distribution in each lattice site. To begin with, we directly map the lattice potential envelope, shown in Fig. 1(b). With the measured potential envelope, we quantify the size and homogeneity of the created potential in Sec. III. In Sec. IV, we use the spectrally resolved carriers to measure local temperatures and the polarizability ratio between the two clock states with high precision. Finally, the monolithic cavity design results in a long atom lifetime in the cavity lattices and an excellent stability of the experimental setup, as discussed in Secs. V and VI.

Our results create new opportunities for quantum simulations of strongly coupled light-matter interfaces [12–14] and quantum chemistry [15]. For such simulations, coherent tunneling over hundreds of lattice sites is desirable [43], which necessitates a large mode area. These simulations also require the creation of state-dependent lattices that trap the clock states with a high contrast ratio and long lifetime [44], which is challenging due to the particularly limited laser power at the necessary wavelengths. Our cavity lattices solve both challenges and also solve the problem of scaling up optical-lattice clocks and neutral-atom quantum computers to tens of thousands of qubits without any changes to the underlying device.

II. EXPERIMENTAL SETUP

A. Crossed cavities

Any optical-lattice experiment faces a trade-off between system size and lattice depth, given by the beam waist and intensity, respectively. Therefore, limited laser power leads to a technical limit on the system size. A natural candidate to increase laser intensities is an optical cavity (or resonator). In a cavity, light circulating between mirrors constructively interferes with incoming light, thus enhancing the laser power circulating within the cavity. Since the power-enhancement factor depends on the mirror reflectivities, whereas a cavity-mode waist depends on the radii of curvature of the mirrors, a cavity provides independent control over the circulating power and waist. This capability lets us achieve deep and large (and thus homogeneous) lattices simultaneously. Other approaches to improve lattice homogeneity use beam shaping via cylindrical lenses [32] or spatial light modulators [31]. However, these approaches face laser power limitations much earlier than power-enhancing build-up cavities.

In contrast to existing build-up cavities, we use a monolithic assembly that is both thermally and mechanically stable [42] to ensure a long-term-stable mode overlap, as

shown in Fig. 1(a). In brief, we optically contact two pairs of 1/2-in. mirrors to an octagon-shaped spacer made from ultra-low-expansion glass, forming two cavities that overlap in the center of the spacer. Our design has no movable parts and is optimized to minimize any potential thermal expansions of the materials that can introduce a relative tilt between the mirrors, which would make the overlap unstable [41,42]. The spacer has bores with different diameters for optical access and high-resolution imaging. With an interferometric method, we achieve a near-perfect vertical overlap between the two modes [41,42].

After construction and characterization, the assembly is mounted in a stainless-steel vacuum chamber attached to the vacuum system [45]. In Fig. 2(a), we show this science chamber, featuring a pair of reentrant view ports that allow high-resolution imaging of the atomic sample. The octagon-shaped cavity assembly is mounted to the top view port in a stress-free manner [41], as sketched in the figure. After bake-out, we reach a pressure below

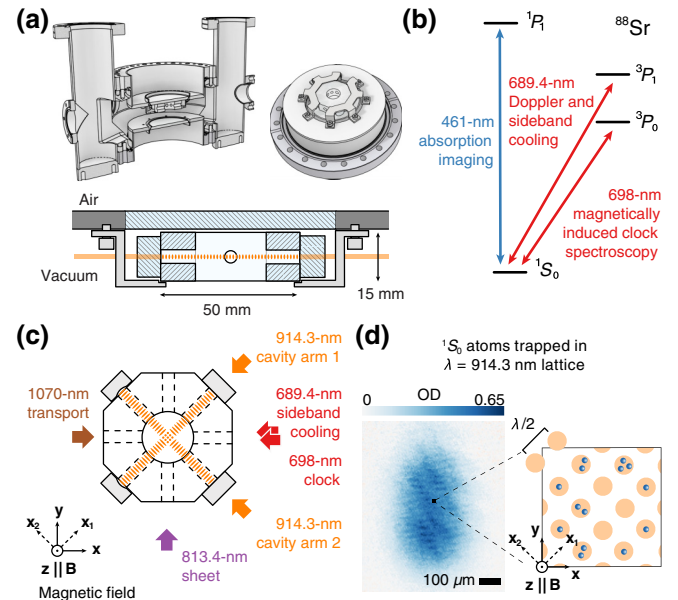


FIG. 2. An overview of the experimental setup. (a) A cross section of the science chamber, which includes a pair of reentrant view ports (top left). The cavity assembly rests in a stainless-steel cage attached to the top view port (top right). A simplified cross-section cut of the cavity assembly and its mounting structure is shown at the bottom. (b) A simplified ^{88}Sr energy diagram and the optical transitions used in the experiment. (c) A sketch of the laboratory and lattice coordinate frames and the relevant laser beams. ^{88}Sr atoms in the $^1S_0(g)$ state are transported into the assembly and are loaded into a trap created by the 914.3-nm cavity-lattice beams and a light sheet at 813.4 nm. The laser beam at 689.4 nm is used for direct sideband cooling and the laser beam at 698 nm drives the clock transition induced by a bias magnetic field B along z . (d) An *in situ* absorption image of g atoms in the combined trap of the lattices and light sheet (left). On the right is an illustration showing the atoms occupying the lattice sites.

3×10^{-11} mbar in the science chamber, demonstrating that the cavity assembly is compatible with state-of-the-art ultra-high-vacuum chambers.

The cavity mirrors are optimized for quantum simulations with strontium atoms and are highly reflective at several selected wavelengths [42]. These wavelengths include 633 nm, 689 nm, 813 nm, 914 nm, and 1064 nm, with power-enhancement factors ranging from 150 to 1132. In the remainder of this work, we couple laser light at 914.3 nm into the cavities. At this wavelength, the finesse and the intracavity power-enhancement factor are 5025(58) and 1132(13), respectively [42]. By coupling a moderate power of approximately 80 mW into each cavity arm, we create deep lattices with trap frequencies of 116 kHz, corresponding to lattice depths of 60 μ K. We optimize the mode-matching of the input beams to the fundamental transverse electric field mode of each cavity (TEM₀₀) to approximately 99% [42]. The laser beams are independently stabilized to the corresponding cavity resonance using acousto-optic modulators (AOMs) as detailed in Appendix A. The cavity lattices are circularly polarized; however, other polarization configurations are also possible since the cavity mirrors are not birefringent.

B. Atomic sample preparation

To benchmark the performance of our optical-lattice setup, we load strontium atoms in the vibrational ground states of the deep cavity lattices. We begin by preparing ⁸⁸Sr atoms using a robust and rapid magneto-optical trap [45] that operates on the narrow 1S_0 - 3P_1 transition, as shown in Fig. 2(b). Subsequently, we transport the atoms into the center of the cavity assembly by moving the focus of an optical dipole trap beam at 1070 nm [46]. The beam propagates along the x axis as shown in Fig. 2(c). Further details about the transport are provided in Appendix A.

After transport, we perform narrow-line Doppler cooling in a crossed-dipole trap. The crossed-dipole trap is created by overlapping the 1070-nm-transport beam and a light sheet at 813.4 nm, as sketched in Fig. 2(c). The elliptical light sheet has a $1/e^2$ beam waist of 400 μ m (13 μ m) along the x (z) axis with a trap depth of 5 μ K, corresponding to trap frequencies of 20, 5, and 500 Hz along the x , y , and z axes, respectively. Here and in the following, the trap depth is understood as the potential energy difference between the center of the trap and the gravity-induced saddle point. Subsequently, the transport beam is turned off and we let the atomic cloud expand in the light sheet.

To adiabatically load the atoms into the cavity lattices sketched in Fig. 2(c), we linearly ramp up the intensity of the cavity beams to a lattice depth (frequency) of 60 μ K (116 kHz). Here, the lattice depth refers to a horizontal modulation depth assuming an infinitely extended 1D lattice, where the lattice trap frequency ν_l and modulation depth V are related by $\nu_l/\nu_{\text{rec}} = 2\sqrt{V}/h\nu_{\text{rec}}$, where $\nu_{\text{rec}} =$

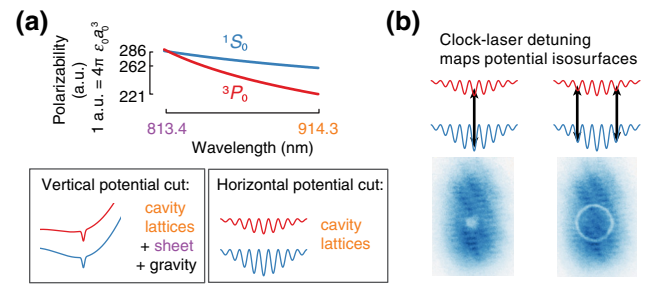


FIG. 3. Spatially dependent clock spectroscopy in nonmagic lattices. (a) The dynamic dipole polarizabilities of the g and e states (top). At the light sheet wavelength of 813.4 nm, g and e have the same polarizability (the *magic* condition). In contrast, at the cavity-lattice wavelength of 914.3 nm, e experiences a polarizability reduced by 15% compared to g (the *nonmagic* condition). For this reason, the light sheet creates identical traps for g and e , while the cavity beams create a slightly stronger potential for g than for e . Vertical and horizontal cuts through the trapping potential created by the light sheet and cavity lattice are sketched below (the polarizability difference between g and e is exaggerated for a clear illustration). (b) *In situ* absorption images after probing the clock transition at different detunings indicated by the black arrows. The differential ac Stark shifts of the nonmagic cavity lattices allow local addressing, leading to ring structures that map the lattice envelope.

$h/2M\lambda^2$ is the lattice-recoil frequency for an atom of mass M and λ is the lattice wavelength. At this point, the atoms are trapped in the potential created by the sheet and cavity beams. The cavity beams by themselves would produce deep lattices horizontally but produce a relatively weak dipole trap vertically with a trap frequency of approximately 50 Hz. Therefore, we achieve a tighter confinement along z by having the light sheet intersect the lattice beams approximately at the minimum of the potential created by the lattice and gravity, as shown in the vertical potential in Fig. 3(a).

After loading the atoms into the lattices, we cool the atoms to the vibrational ground band using sideband cooling on the 1S_0 - 3P_1 transition [47,48], where the 689.4-nm cooling beam propagates horizontally at 45° to the lattice axes, as sketched in Fig. 2(c). Then, we ramp down the lattice power after sideband cooling to drop the atoms that are trapped only by the lattices but not by the light sheet and we ramp the lattices back up. Subsequently, we measure in-trap density profiles with *in situ* absorption imaging along z [45]. In Fig. 2(d), we show a typical absorption image. We use a large field of view and low-resolution imaging with 5.40(8) μ m per pixel to image the large atomic distribution and we do not resolve the lattice structure. Based on the optical density, we expect an average atom number of approximately 1 per lattice site at the center of the trap.

C. ⁸⁸Sr clock excitation

We perform high-resolution spectroscopy on the ultranarrow clock transition between 1S_0 (g) and 3P_0 (e) of

strontium, as shown in Fig. 2(b). Unlike in the fermionic isotope ^{87}Sr , where the clock transition is weakly electric dipole allowed [49] with a linewidth of 1.35(3) mHz [50], accessing the transition of the bosonic isotope ^{88}Sr requires an external magnetic field [51]. Despite this requirement, we use ^{88}Sr , because of its high natural abundance and simple electronic structure, which leads to simpler spectroscopic features.

To perform clock spectroscopy, we merge a 698-nm clock probe beam into the same optical path as the 689.4-nm sideband cooling beam, as sketched in Fig. 2(c). We apply clock-laser light for approximately 600 ms and a bias magnetic field of approximately 45 G parallel to z , unless specified otherwise. The clock probe beam has a $1/e^2$ waist of approximately 285 μm and a power of 21 mW, where the waist has been calibrated as in Ref. [44].

The cavity lattices are created at a wavelength of 914.332 nm. At this wavelength, the differential polarizability of the clock states $\alpha_g - \alpha_e \simeq 0.15\alpha_g$, as is evident from the polarizability plots of g and e shown in Fig. 3(a). Here, α_k specifies the polarizability of a state k . The differential light shift is proportional to the light intensity and the differential polarizability. As a result, the clock-transition frequency shifts and the magnitude of the shift varies as a function of the lattice intensity. Lattices in which the two clock states experience different light shifts are called *non-magic*. In contrast, we intentionally make the light sheet operate at the *magic* wavelength of 813.4 nm, such that it does not shift the transition. Therefore, the local clock shift only originates from the cavity beams. The trapping potential for g and e created by the combination of cavity beams, the light sheet, and gravity is illustrated in Fig. 3(a). In the vertical potential cut, we see a dimple created by the 813.4-nm sheet and its trap depth is identical for both g and e . The horizontal potential cut is dominated by the cavity beams and e experiences a weaker lattice depth than g . Therefore, we see that only the cavity lattices determine the differential light shift in the horizontal plane.

We model the cavity light intensity as the sum of two orthogonal TEM_{00} Gaussian beams with $1/e^2$ waist w . We assume that the waist of both cavity modes is the same because the two cavities are constructed in the same way [42]. We also assume that the waist stays constant over the area of our interest, which is valid because of the long Rayleigh length of the beams, $z_R \sim 80$ cm. When the clock-laser frequency is tuned close to the maximum differential ac Stark shift, we excite g atoms in the center as illustrated in Fig. 3(b). In contrast, when the laser is red detuned from the maximum, we excite g to e in an equipotential region. This region takes the shape of a ring, reflecting the spatial cross section of the light intensity. Taking such cross sections at different detunings enables us to map out the lattice trap envelope created by the cavity beams.

III. CHARACTERIZING THE LATTICE ENVELOPE

We use the measured equipotential surfaces to characterize the waist and homogeneity of the potential. At each clock-laser detuning δ , we take two absorption images which measure the optical density (OD) of the atomic sample. The first image is taken without clock excitation (OD_{bg}), and the second image is taken with clock excitation (OD_{clk}). From these two images, we extract a normalized difference image, $(\text{OD}_{\text{bg}} - \text{OD}_{\text{clk}})/\text{OD}_{\text{bg}}$, and reconstruct the potential map as illustrated in Fig. 4(a). This postprocessed image reflects the fraction of g atoms that have been *depleted* by the clock excitation. Here, the *depleted atoms* include both those atoms that are still in e at the time of imaging and those that have been lost from the trap after the excitation due to inelastic excited-state collisions [52,53]. The details of the excitation process are described in Appendix A. We use this postprocessed image representing the depleted ground-state fraction for further analysis to eliminate possible systematic errors originating from the initial density distribution.

From a series of postprocessed images taken at different detunings δ , we determine the resonant detuning δ_{res} of each pixel, which is proportional to the lattice envelope averaged over each pixel. Example traces of the fractional depleted g atoms of a pixel are shown in Fig. 4(b). Each trace is individually fitted to a Lorentzian line shape to extract δ_{res} for its pixel. The distribution of the reduced χ^2 of all the fits is centered around 0.9 and the statistical error on δ_{res} from the fits is approximately 100 Hz. The image of δ_{res} maps the shape of the potential and is shown in Fig. 4(c). The variation of the potential depth across the whole image is approximately 10% of the total ac Stark shift, since we only load atoms into the central lattice region.

To quantify the waist and deviation of the measured δ_{res} from the expected values, we fit the image of δ_{res} to a fitting function that models the potential given by the superposition of two orthogonal TEM_{00} cavity modes. The details of the fitting function and fit parameters are described in Appendix C. We perform a weighted-least-squares fit and obtain a cavity-mode waist of 489(8) μm , where the uncertainty arises mostly from the uncertainty in the image-system magnification. Although the fit captures the global Gaussian shape well, the residuals reveal that there are additional fringes shown in Fig. 4(d). Since the peak-to-peak amplitude of the most dominant fringe (approximately 3 kHz) is an order of magnitude larger than the error on the δ_{res} estimates (approximately 100 Hz), the fringes are well resolved. The statistical uncertainties show that our method can resolve structures as small as 300 parts per million (ppm) of the total ac Stark shift. Due to the additional inhomogeneous fringes, the reduced χ^2 of the lattice envelope fit to the δ_{res} data is approximately 5 and

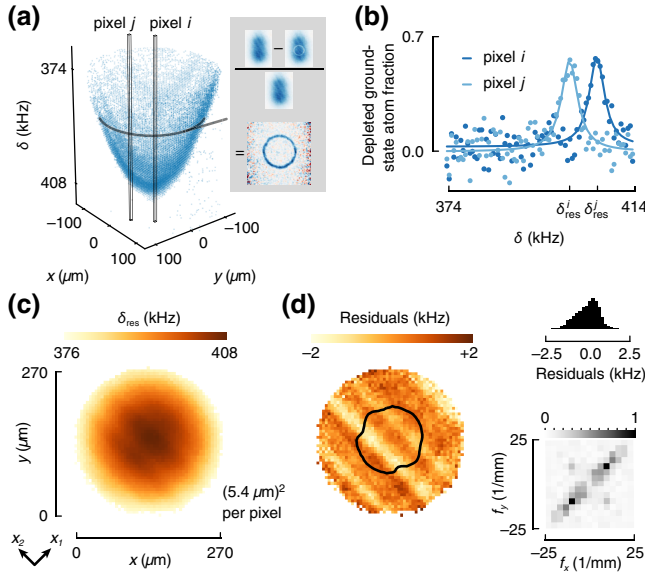


FIG. 4. Lattice envelope characterization. (a) The envelope of the lattice potential reconstructed by stacking the images of depleted g fractions obtained at different clock-laser detunings δ (left). To obtain these images, we take an image with (OD_{clk}) and without (OD_{bg}) clock excitations. For each detuning, we calculate the depleted g fraction $(\text{OD}_{\text{bg}} - \text{OD}_{\text{clk}})/\text{OD}_{\text{bg}}$ (right). (b) For every pixel, we plot the depleted g fraction as a function of the detuning δ and extract the peak frequency δ_{res} with a Lorentzian fit (solid lines). (c) The resulting image of δ_{res} for every pixel in (a). The cavity axes are labeled as x_1 and x_2 . (d) When fitting the potential envelope predicted by ideal TEM_{00} modes to the data in (c), we find fit residuals showing fringe patterns coaligned with the lattice axes. A histogram (peak-normalized spatial Fourier transform) of the residuals is shown in the top (bottom) right. The black contour line on the image of residuals shows the expected Mott-insulator shape, based on the envelope data in (c). The resulting shape is shown as the shaded region in Fig. 1(b).

the histogram of residuals is asymmetric, as shown at the top right of Fig. 4(d).

We observe that the inhomogeneous fringes are well aligned with the cavity axes and that they are more (less) pronounced parallel to the optical axis of cavity arm 2 (arm 1), corresponding to lattice coordinate x_2 (x_1), as defined in Fig. 2(c). We characterize the fringe spacings using the peak-normalized 2D Fourier transform of the zero-padded fit residuals. The result is shown at the bottom right of Fig. 4(d) and reveals a factor-of-3-larger fringe amplitude along coordinate x_2 compared to x_1 , peaking at a fringe wavelength of approximately $65 \mu\text{m}$. Despite the different magnitudes, the Fourier transform shows similar spatial frequency components along both axes. This similarity in the frequency components strongly suggests that a common mechanism causes the fringes along both axes.

The presence of these fringes is surprising, since the mode-cleaning effect of the cavities is expected to lead to a clean potential. The first obvious question is whether the fringes are truly present in the optical potential. We lay

out three potential scenarios in Appendix D and conclude that all three scenarios are highly unlikely. Determining whether the fringes are present in the cavity lattices or whether they are artifacts of the detection method requires further investigation using a combination of improved beam shaping and alternative detection methods such as site-resolved fluorescence imaging. For the remainder of this work, we assume that the fringes are present in the potential and show that even under this worst-case assumption, the cavity lattices outperform all other existing solutions for scaling up 2D optical lattices.

To our knowledge, we have created the largest far-off resonant 2D optical lattices for trapping ultracold atoms. Our cavity-mode waists are more than 5 times larger than what can be created using the most powerful laser available at this wavelength while preserving the lattice depth, resulting in an improvement of more than an order of magnitude in the number of available lattice sites. From the measured intensity profile, we estimate an achievable Mott-insulator size for the fermionic isotope ^{87}Sr , which has more suitable scattering properties than the bosonic isotope ^{88}Sr . In two dimensions, the interaction energy U required to form a Mott insulator is approximately $8t$, where t is the tunneling rate [11]. For a fixed scattering length, the lattice depth can be tuned to satisfy the condition mentioned above. At a typical depth of approximately $10h\nu_{\text{rec}}$, a Mott insulator forms within the region where the energy shift due to the lattice envelope is smaller than the interaction energy between two atoms. We find that the peak-to-peak amplitude of the fringes is 3 times smaller than the interaction energy, which is approximately 700 Hz for ^{87}Sr . Therefore, we expect a homogeneous Mott insulator extending up to the boundary set by the interaction energy. The fringes cause small distortions of the Mott-insulator shape, as shown in Fig. 4(d). However, our results show that the size would not significantly differ from the ideal size created with perfectly homogeneous lattices.

From these estimates, which are detailed in Appendix B, we expect that the Mott-insulator state will occupy a region with a diameter of $D \simeq 125 \mu\text{m}$ at a wavelength $\lambda = 914.3 \text{ nm}$. This diameter corresponds to $N \simeq \pi(D/\lambda)^2 \simeq 6 \times 10^4$ lattice sites. The area of the region does not vary much as a function of the wavelength λ , although the number of sites changes quadratically due to the change in lattice spacing. For this reason, our cavity assembly offers a solution to the creation of large Mott insulators at any wavelength of interest [26,44] supported by the cavity mirrors.

IV. LOCAL CLOCK SPECTROSCOPY IN NONMAGIC LATTICES

In Sec. III, the discussion focuses on driving the most dominant carrier transition between the lowest vibrational

states of the g and e lattices. The carrier spectrum discussed in Fig. 4(b) is modeled with a Lorentzian function. However, the spectrum can become more complex when transitions between higher vibrational states are considered. We now make use of the high spectral resolution of the clock laser to resolve spectral transitions between such higher vibrational states. This new capability enables us to precisely determine the polarizability ratio of the clock states without having to calibrate the lattice intensities. This ratio is an important quantity that determines the magnitude of the differential light shift and can be used to calibrate state-of-the-art atomic structure calculations [44]. Moreover, we find that we can use this method to locally measure temperature with a spatial resolution only limited by the imaging optics.

To understand the spectra that we measure, we first consider the sideband spectrum in a deep optical lattice, where tunneling is suppressed. In this case, the spectrum resembles the spectrum of a harmonically trapped ion [47] and a trapped atom occupies a discrete vibrational level n . Assuming an infinitely extended 1D lattice without any radial confinement and considering the quartic distortion by the sinusoidal lattice potential, the vibrational energy spectrum is [54]

$$E_n/h = \nu_t \left(n + \frac{1}{2} \right) - \frac{\nu_{\text{rec}}}{2} (n^2 + n + 1), \quad (1)$$

where ν_t is the on-site lattice trap frequency. With this expression, we can explain all the spectral transitions observed in atoms trapped in a deep nonmagic optical lattice.

A typical spectrum consists of three different types of transitions: carrier transitions that maintain the vibrational state and red- and blue-sideband transitions that, respectively, remove and add a motional quantum. In a magic wavelength lattice, the transition frequencies of all carrier transitions are degenerate. From Eq. (1), we find that the first red- and blue-sideband transitions are detuned from the carrier by $\nu_t - \nu_{\text{rec}}$. Typically, the sideband transitions are highly suppressed compared to the carrier transitions by the Lamb-Dicke factor [47]. The red sideband is even further suppressed in a laser-cooled sample due to a large ground-vibrational-state population. In this work, we focus on the carrier and the first blue-sideband transitions.

The spectrum becomes more complex in a nonmagic lattice, where the trap potential is state dependent. Thus, the trap frequencies of the g and e lattices are different and we use ν_t^k to denote the trap frequency of state k . In this case, the carrier transitions are no longer degenerate but are split by $\nu_t^e - \nu_t^g$ according to Eq. (1). Moreover, the first blue sideband is detuned by $\nu_t^e - \nu_{\text{rec}}$ from the carrier transition of the lowest vibrational state.

In 2D, the vibrational levels are labeled by two independent vibrational numbers n_1 and n_2 , each corresponding

to a vibrational band of one of the lattices. Since the two lattices are orthogonal and do not interfere, the energy spectrum is given by $E_{n_1} + E_{n_2}$. For simplicity, we consider the case when both lattices have an equal intensity (or depth), $I = I_1 = I_2$. In this case, the carrier transitions split according to the total vibrational number $n_T = n_1 + n_2$ of the states involved. Therefore, each carrier transition is (n_T+1) -fold degenerate. An example of a coarse scan over the clock-excitation spectrum for $\nu_t^e \simeq 77$ kHz in our nonmagic 2D lattices is shown in Fig. 5(a).

We work in a resolved carrier regime that has not been previously explored. The frequency splitting between the two neighboring carrier transitions is $(\nu_t^g - \nu_t^e) \propto \sqrt{I}(\sqrt{\alpha_e} - \sqrt{\alpha_g})$. To maximize the splitting, we increase ν_t^e to approximately 109 kHz and take a high-resolution spectrum of the carrier transitions as shown in the left part of Fig. 5(b). We observe up to three different carrier transitions, of which the one from the lowest vibrational state is the most blue detuned. The amplitude of the three peaks becomes more comparable when we intentionally heat the sample by applying a beam resonant with the 1S_0 - 3P_1 transition, as shown in the right part of Fig. 5(b). As we decrease the lattice depth linearly, we observe that the splitting reduces quadratically as expected. Similar to the carrier transitions, the first blue-sideband transitions split as well. However, here we focus on the first blue sideband of the lowest vibrational state, which is shown in Fig. 5(c).

The splitting of the carrier transitions is clearly visible in the ground-state images as well. As described in Sec. III, we excite atoms in a ring shape, reflecting the equipotential surfaces of the cavity-lattice envelope. When we increase the population of the higher vibrational states by heating the sample, we see additional smaller rings appearing in Fig. 5(d). Each ring results from driving the carrier transitions from different vibrational states, which are resonant at different locations. Similar to what we have seen in Sec. III, all three rings move inward as the detuning increases due to the spatially dependent ac Stark shift. The dominant carrier transition, which involves the lowest vibrational states, arrives at the center last because it is the most blue-detuned transition. Moreover, the spacing between two neighboring rings increases as the rings approach the center, since the potential becomes flatter.

With the resolved carrier and blue-sideband spectrum, we first extract the polarizability ratio α_g/α_e , which is one of the parameters that determine the magnitude of the differential ac Stark shift. Since $\alpha_k \propto (\nu_t^k)^2$, the polarizability ratio $\alpha_g/\alpha_e = (\nu_t^g/\nu_t^e)^2$. To measure ν_t^e and ν_t^g , we use an analysis method similar to the one used in Sec. III. For every two-by-two averaged pixel, we determine the frequency difference between the lowest carrier and first blue-sideband peaks, which is $\nu_t^e - \nu_{\text{rec}}$. To measure ν_t^g , we heat the sample to better observe the different carrier peaks. For each spectrum of the averaged pixel, we fit a three-peak Lorentzian function, with the frequency difference between

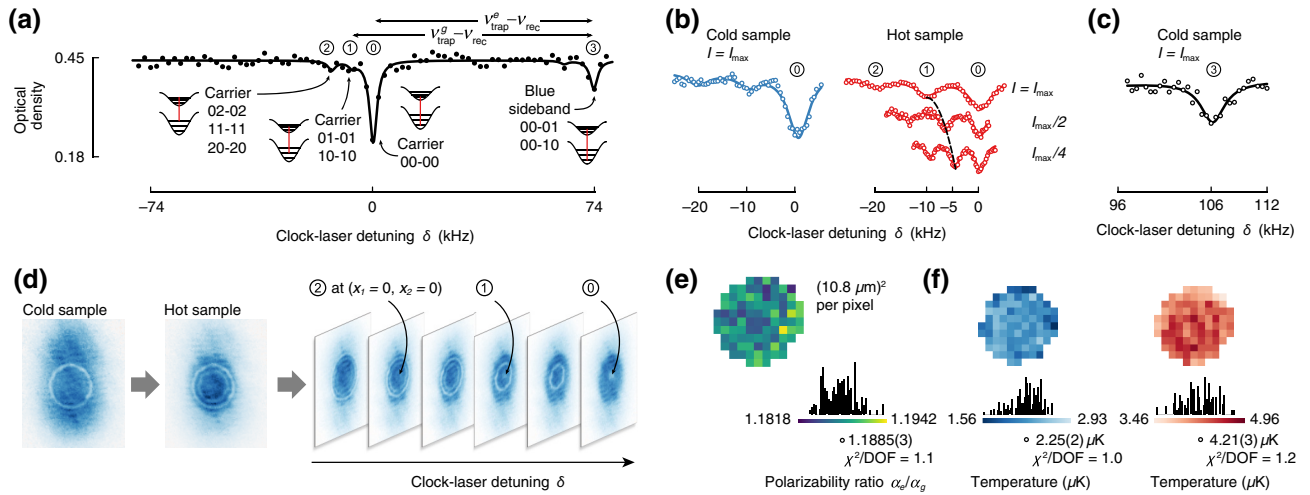


FIG. 5. The local clock spectroscopy of carrier and sideband transitions in nonmagic lattices. (a) A sparse clock-sideband spectrum in a 2D nonmagic optical lattice. The solid line is a fit to a multipole Lorentzian function, in which the peak locations are fixed at the expected detunings. (b) A more finely resolved spectrum covering a detuning range of the carrier transitions for the samples with two different temperatures, one colder (left) and the other hotter (right). To maximize the splitting, we increase ν_t to approximately 109 kHz from approximately 77 kHz [at which (a) is taken]. For the hotter samples, we vertically stack three spectra taken at different lattice intensities I , at which I_{\max} results in $\nu_t \simeq 109$ kHz. The dotted line is a guide to the eye for easier visualization of the carrier splitting frequency as a function of the lattice intensity. (c) A blue-sideband spectrum taken at $\nu_t \simeq 109$ kHz. (d) A comparison of the absorption images of the cold and hot samples after the clock excitation at a fixed detuning (left) and a series of images of the hot sample as a function of the detuning. (e) The per-pixel polarizability ratio and weighted histogram. (f) Temperature maps of cold (left) and hot (right) samples with weighted histograms, where DOF stands for the degrees of freedom of the corresponding fit.

the peaks constrained to be the same. From the fit, we determine the frequency splitting $\Delta\delta$ between the carriers for each averaged pixel and combine this value with ν_t^e to obtain ν_t^g for every pixel, $\nu_t^g = \nu_t^e + \Delta\delta$. The error bars of the parameter estimates from the fits are rescaled according to the reduced χ^2 of the fits to compensate for the non-Gaussian noise of the absorption images.

In Fig. 5(e), we show the polarizability ratio estimated from the pixel-to-pixel ν_g and ν_e maps. The weighted mean of the ratio $\alpha_g/\alpha_e = 1.1885 \pm (3 \times 10^{-4})_{\text{stat}} \pm (1 \times 10^{-3})_{\text{sys}}$, which is in good agreement with the theory described in Appendix E. The systematic uncertainty arises from the experimental drifts between the hot and cold data sets that are used to extract ν_e and $\Delta\delta$, respectively. This uncertainty can be greatly reduced by further minimizing the elapsed time between the data sets. The variance of the ratio across the sample can be explained by the variance of each pixel because the reduced χ^2 is 1.14. Therefore, we conclude that we do not observe a systematic variation of the ratio across the sample. Our method provides improved robustness compared to a similar method explored in Ref. [55] because we can make use of the resolved carrier spectrum combined with spectral imaging.

Finally, we extract the local temperatures of the sample using the carrier spectrum. In the temperature regime that we are considering, the vibrational populations are Boltzmann distributed. In this case, the temperature T can be estimated by measuring the relative population p_0/p_1 of

the first two nondegenerate levels and the energy spacing between them, using $k_B T = \hbar(\nu_t^g - \nu_{\text{rec}})/\ln(2p_0/p_1)$. We estimate $\nu_t^g - \nu_{\text{rec}}$ for each pixel using the same method as described above. Next, we use a hotter sample and determine the peak locations and amplitudes by fitting a three-peak Lorentzian function with an equal frequency difference between the peaks to each averaged pixel and we compare the amplitudes of the two most blue-detuned carrier peaks to estimate p_1/p_0 . For the colder sample, we repeat the same procedure but keep the peak locations fixed to those determined from the hotter sample.

The extracted temperature maps and weighted histograms are shown in Fig. 5(f). We clearly observe a temperature difference between the cold and hot samples at $2.25(2) \mu\text{K}$ and $4.21(3) \mu\text{K}$, respectively. The temperature variations across the samples are within the temperature uncertainty of each pixel because the reduced χ^2 is 1.01 and 1.2 for cold and hot samples, respectively. The temperatures of the cold sample correspond to an approximately 80% vibrational ground-state fraction.

Our local thermometry assumes that the induced atom losses during the clock excitation (discussed in Appendix A) do not influence the temperature estimates. This assumption is corroborated by repeating the temperature measurements with shorter clock-excitation durations and negligible loss, where we do not observe temperature differences. The thermometry technique based on the carrier spectrum has been proven to be more precise

than methods based on time of flight or the sideband spectrum due to its high signal-to-noise ratio [55,56]. We improve the robustness of the technique by resolving the carriers and extending it to probe local temperatures. When combined with higher numerical aperture imaging, this technique will enable spectroscopic measurements of motional-band populations with single-site resolution.

V. LIFETIME

In optical traps, heating induces excitation to higher motional bands, leading to motional-state decoherence and subsequent atom loss. To characterize the heating sources in our setup, we measure the lifetimes of the ground-band population and the overall lifetime of atoms trapped in the cavity lattices.

We characterize the ground-band lifetime using the resolved-carrier-spectrum technique presented in Sec. IV. This technique offers a new way to probe the motional ground-band populations in the high-lattice-depth regime with a high signal-to-noise ratio. In Fig. 6(a), we take two carrier spectra after holding the atoms in the lattices at a modulation depth (trap frequency) of $457 E_{\text{rec}}$ (116 kHz) for 1 s and for 15 s. By comparing the populations in the ground band at these times and assuming an exponential heating rate, we extract a ground-band lifetime of 18(3) s, which is comparable to state-of-the-art free-space lattice experiments [57] at similar depths in units of the recoil energy.

In addition to the ground-band lifetime, we also measure the overall trap lifetime at the same lattice-modulation depth. The overall trap lifetime serves as a good benchmark to compare with other setups where the ground-band lifetime is not accessible. In Fig. 6(b), we show the number of g atoms trapped in the cavity lattices and the light sheet as a function of the trap hold time and we extract a trap $1/e$ lifetime of 59(2) s.

The heating mechanisms in optical traps include collisions with background gas, incoherent scattering of trap light, and laser-noise-induced heating [57]. Based on the longest trap lifetime that we measure, we project a vacuum-limited lifetime > 180 s. The expected lifetime due to incoherent light scattering is also more than 2 orders of magnitude longer than the observed ground-band lifetime, leaving laser noise as the main source of heating. Moreover, we observe that the lifetime changes depending on the parameters of the intensity and frequency-stabilization control loops of the laser.

Laser-noise-induced heating arises due to laser-beam intensity and pointing fluctuations. In deep optical lattices, where each lattice site can be approximated as a harmonic trap, the laser-intensity (pointing) noise power spectral density at $2\nu_l$ (ν_l) causes parametric heating [58] that results in transitions between lattice bands that are two (one) motional quanta apart. In traps enhanced by

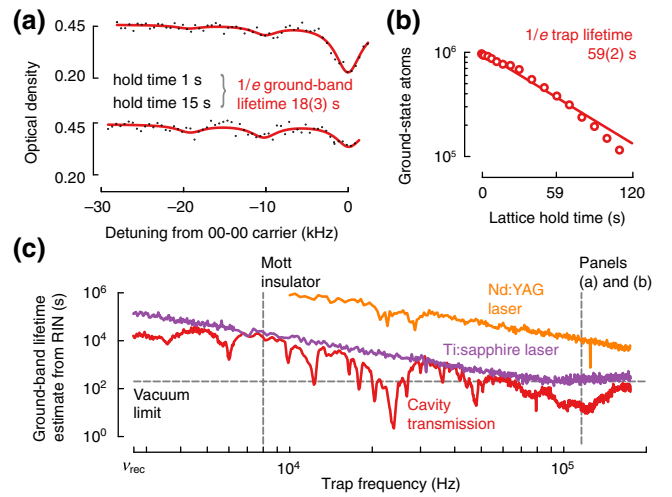


FIG. 6. The lifetime in the cavity lattices. (a) Resolved carrier spectra in the cavity lattices at a trap depth (frequency) of $457 E_{\text{rec}}$ (116 kHz). The spectrum on the top (bottom) is taken after holding atoms for 1 s (15 s) in the lattices. We extract a $1/e$ lattice-ground-band lifetime of 18(3) s. (b) The number of g atoms as a function of the lattice hold time. We extract an overall $1/e$ trap lifetime of 59(2) s. (c) The estimated ground-band lifetime of different laser sources as a function of the lattice depth. Here, we consider three different sources: a Ti:sapphire laser (purple), which is the input light to the cavity; a Ti:sapphire laser transmitted through cavity 2 (red); and a high intensity-stable Nd:YAG laser (orange). Our lifetime measurement at a trap depth (frequency) of $457 E_{\text{rec}}$ (116 kHz) shown in (a) and the relative-intensity-noise (RIN) measurements of a Ti:sapphire laser transmitted through cavity 2 at this trap frequency provide a reference value. The estimation is performed by rescaling the RIN of these laser sources with respect to this reference value.

optical cavities, we expect the intensity fluctuations to dominate for three reasons. First, heating from pointing fluctuations is strongly suppressed due to the mechanical stability of the resonator [59]. Second, locking a laser to a cavity resonance converts laser-frequency noise into amplitude noise, increasing the latter beyond that in free-space optical lattices [60]. Third, any pointing fluctuations of the cavity input beam, or fast cavity-length changes induced by mechanical noise (outside of the bandwidth of the control loop) get converted to fluctuations of the cavity-lattice depth. However, the cavity-lattice depth fluctuations are straightforwardly accessible by measuring the relative-intensity noise (RIN) of the cavity transmission.

By combining the transmission-RIN and ground-band-lifetime measurements, we estimate expected lifetimes for different lattice depths as shown in Fig. 6(c). Here, we use the parametric heating rate $\propto \nu_l^2 S(2\nu_l)$, where $S(2\nu_l)$ is the power spectral density of the fractional intensity noise at $2\nu_l$, to scale the lifetimes to the measurement shown in Fig. 6(a), based on the model in Ref. [57]. However, based on the rescaled RIN of the transmission, we estimate

that the ground-band lifetime will be vacuum limited in the low-lattice-depth regime, even at wavelengths where very-low-noise non-planar-ring-oscillator lasers [61] are not available.

VI. LONG-TERM STABILITY

Finally, we characterize the long-term frequency and intensity stability of the lattice beams. In our setup, the lattice laser is stabilized to a resonant frequency of the cavity, which slowly changes as the cavity shrinks or expands. Since we do not actively stabilize the cavity length, any length change directly influences the laser frequency. Although we actively stabilize the input beam power before coupling it into the cavity, we do not additionally stabilize the power of the transmitted light. Therefore, the beam power inside the cavity is susceptible to mechanical drifts of the incoupling optical components and the performance of the input intensity servo. In this section, we quantify the frequency and intensity drifts of our setup and discuss the consequences for optical-lattice clocks and quantum simulators using our cavity lattices.

To estimate the laser-frequency drift due to the cavity-length change, we continuously measure two parameters: (i) the laser frequency by beating it with a femtosecond optical-frequency comb and (ii) the frequency of the double-pass AOM used to stabilize the laser to the cavity resonance frequency (Appendix A). By subtracting the one number from the other, we obtain the resonance-frequency drift of the cavity independently of the laser-frequency drift. In Fig. 7(a), we plot the change of the resonance frequencies for both cavities as a function of time, starting with the moment we couple light into the cavities. We use a circulating power of approximately 92 W in each cavity, matching the conditions of the measurements in Secs. III–V. Within the first hour, we observe a rapid decrease in the resonance frequency of approximately 6 MHz. Subsequently, the resonance frequencies settle but fluctuate with a peak-to-peak amplitude of approximately 2 MHz.

The decrease by 6 MHz corresponds to a cavity expansion of 1 nm compared to the nominal cavity length of 50 mm. When repeating this measurement at different power levels, we see that the expansion reduces proportionally (see inset). We conclude that the cavity mirrors scatter and absorb part of the circulating light due to the cavity-mirror losses, which are approximately 100 ppm based on our finesse and transmission measurements. These losses deposit heat on the cavity which therefore expands. We attribute the fluctuations on the long time scales to slow environmental temperature changes, which could be further reduced by stabilizing the temperature of the vacuum chamber.

We use the measured resonance stability to estimate a lower bound of the accuracy of an optical-lattice clock

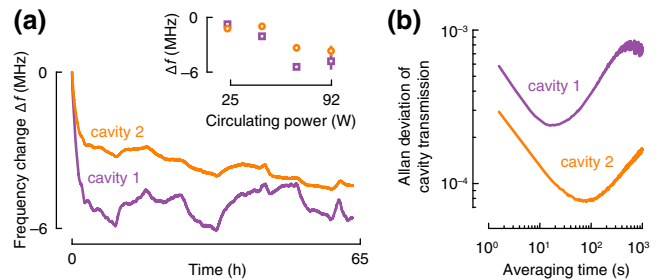


FIG. 7. The stability of the cavity lattices. (a) The change in the cavity resonance frequency Δf as a function of time for both cavities. At $t = 0$, we couple the laser beams into the cavities, which create a circulating power of approximately 92 W per cavity. We see a rapid initial decrease of 6 MHz, which corresponds to an expansion of the cavity length by 1 nm. Then, Δf settles and fluctuates with a peak-to-peak amplitude of approximately 2 Hz. The inset shows Δf as a function of the circulating power for cavity 1 (squares) and 2 (circles). Here, Δf is extracted by fitting the trace of the first hour to an exponential function. (b) The fractional intensity variation of the cavity transmission plotted as a function of time.

based on our cavities. Compared to cavities that are tunable in length [25,39,59,62,63], we have to overcome the obstacle of constructing a fully monolithic cavity with resonances as close to the magic wavelength as possible. This problem could be solved by adapting our optical contacting methods [41] to tune the resonance frequency with an accuracy of 10 MHz. The cavity resonance frequency can be further fine tuned by placing it in a temperature-controlled enclosure, which is also required to create a well-defined black-body-radiation environment [39,64]. To estimate the clock inaccuracy due to detuning from the magic wavelength condition, we assume a lattice depth of $100 E_{\text{rec}}$ [65], which leads to a cavity-frequency variation of approximately 1.3 MHz caused by coupling light into the cavity. With these assumptions, we obtain a clock-frequency variation of 2 mHz [66], corresponding to a fractional clock accuracy of approximately 5×10^{-18} . We believe that the largest contribution to the cavity-frequency variation is the mirror loss, which can be reduced by more than an order of magnitude when using mirrors with < 10 ppm loss. This reduction would improve the frequency stability by an order of magnitude, assuming that reducing the mirror loss would proportionally reduce the cavity-frequency variation. The necessary temperature control to minimize the black-body-shift uncertainty reduces the frequency fluctuations caused by environmental changes to the same level. Other systematic effects such as charge build-up on dielectric surfaces and a nonuniform black-body-radiation background due to the cavity spacer can be addressed using existing techniques. Charge build-up can be reduced by placing electrodes on the inside of the central cavity bore to compensate for stray electric fields and to evaluate the magnitude of the stray field

[39]. Black-body-radiation shifts can be suppressed by providing a temperature-controlled environment [39,64] at low temperatures [67,68]. With these improvements, we project a possible clock accuracy below 10^{-18} , which would let state-of-the-art 2D or 3D optical-lattice clocks make use of the scaling advantage provided by our cavity lattices.

Finally, we characterize the long-term stability of the cavity-lattice depth by measuring the cavity transmission. The Allan deviation of the transmitted power as a function of the averaging time is shown in Fig. 7(b). We observe a fractional instability below 10^{-3} for typical approximately 20 s cycle times of quantum gas microscope experiments. Furthermore, the transmission of cavity 2 is more stable than that of cavity 1, which is consistent with the lower input-power sensitivity observed in Fig. 7(a). By measuring the transmission and implementing a slow feedback loop on the cavity input powers, we could preserve the stability over many experimental runs, which would result in long-term-stable quantum simulation parameters. The fractional stabilities of the tunneling rate t and the interaction energy U roughly scale as $(3/4)(\sigma_V/V)$, where σ_V/V is the fractional uncertainty of the lattice depth V . Therefore, we expect that it is feasible to achieve a long-term stability of 10^{-3} for t and U .

VII. CONCLUSIONS

We present a new cavity-based experimental platform for scaling up the number of qubits for quantum simulators, quantum computers, and clocks based on neutral atoms trapped in optical lattices. Our lattices increase the number of available lattice sites by more than an order of magnitude compared to state-of-the-art free-space lattices [57]. Currently, most far-off-resonant optical lattices are created using high-power Nd:YAG lasers. Here, our solution opens up new opportunities to create large and deep lattices at any desired wavelength supported by the cavity-mirror coatings.

As a demonstration, we load strontium atoms into 2D optical lattices generated at 914.332 nm, which is well adapted for narrow-line laser cooling of strontium atoms. The lattice laser beams have waists of $489(8) \mu\text{m}$ and operate at a circulating power of 92 W. This circulating power is more than an order of magnitude larger than commercially available laser power at this wavelength. Despite the large beam waist, atoms are trapped in lattices as deep as $457 E_{\text{rec}}$, corresponding to trap frequencies of 116 kHz. In these nonmagic optical lattices, we perform high-resolution clock spectroscopy. Extending the work of Refs. [69,70], we show a highly sensitive method to reconstruct the lattice-intensity envelope from the local clock shift. The statistical uncertainty of our reconstruction method shows that intensity deviations as small as 300 ppm of the peak intensity can be resolved. From the

reconstructed intensity map, we estimate the size and shape of a future Mott-insulator state and conclude that the state will consist of 6×10^4 atoms. This atom number is more than an order of magnitude larger than in state-of-art 2D optical lattices generated from free-space laser beams [57].

The combination of high-resolution laser spectroscopy and deep nonmagic lattices allows us to resolve different motional carrier transitions of the lattices for the first time. We use this capability to locally measure the sample temperature with high spatial resolution. The resolved carrier spectrum also provides a method to directly measure the ground-band lifetime. We observe ground-band and lattice lifetimes of 18(3) s and 59(2) s, respectively, and a long-term lattice frequency (depth) stability on the megahertz (0.1%) level. Our results demonstrate that there are no disadvantages of cavity-based far-off-resonant optical lattices compared to free space, while allowing the creation of deep and large optical lattices at wavelengths where the available laser power is limited. These cavity lattices create new opportunities for analog and digital quantum simulation, including controlled collisional phase gates [71–73], quantum simulations of light-matter interfaces [12,13,43,74] and quantum chemistry [15]. Moreover, the strong reduction in harmonic confinement will reduce the finite-size effects for any optical-lattice quantum simulator and will reduce the experimental time required for measuring quantum many-body correlations.

The cavity lattices can also be used to improve the precision of lattice-based atom interferometers and optical-lattice clocks by providing more identical particles to reduce the quantum projection noise. Our compact and stable cavity design will enable near-future applications of optical atomic clocks that require hands-off operation outside of laboratories, such as in satellites and airplanes [75–78]. Finally, neutral atom arrays in optical tweezers interacting via Rydberg states have become a promising candidate for quantum computing [4–7] but current array sizes have been limited to approximately 400 sites, partly due to the high laser power required to create larger arrays [79]. With our optical-cavity lattices, these neutral-atom quantum computers can be scaled to tens of thousands of qubits.

ACKNOWLEDGMENTS

We thank M. Safronova for providing the matrix elements required for the polarizability-ratio calculation and for stimulating discussions and D. Yankelev for critical reading of the manuscript. This work was supported by funding from the European Union [“Programmable Atomic Large-Scale Quantum Simulation” (PASQuanS) Grant No. 817482]. A.J.P. was supported by a fellowship from the Natural Sciences and Engineering Research Council of Canada (NSERC), funding ref. no. 517029, N.Š. was supported by a Marie Skłodowska-Curie

individual fellowship (Grant Agreement No. 844161), and V.K. was supported by a Hector Fellow Academy fellowship.

APPENDIX A: EXPERIMENTAL DETAILS

1. Crossed-cavity locks

The cavity-lattice beams at 914.332 nm are generated from a Ti:sapphire laser. The output of the laser is divided into four paths: a path for locking the frequency of the laser to a prestabilization cavity, two paths for coupling into each cavity arm of the crossed-cavity assembly, and an optical-heterodyne-beat setup with a femtosecond optical-frequency comb. Locking the frequency of the laser to a prestabilization cavity with a piezo-tunable length allows us to keep the frequency of the laser close to the resonance frequencies of the crossed cavities.

The length of the prestabilization cavity is actively stabilized by locking one of the resonance frequencies to the clock-laser frequency with a Pound-Drever-Hall (PDH) lock. The clock laser itself is frequency stabilized to an ultrastable reference cavity with a finesse of approximately 280 000. Once the length of the prestabilization cavity is stabilized, we lock the frequency of the Ti:sapphire laser to another of its resonances via the PDH technique as well. For this purpose, the error signal is fed back to a piezo attached to the bow-tie cavity mirrors of the Ti:sapphire laser.

The two beams that couple into the cavities are each frequency shifted with separate double-pass AOMs and then fiber coupled to the optical setup for coupling into the cavities. The AOMs tune the frequency of each beam to the resonant frequency for each cavity. To maintain the desired frequency for each beam, we again use the PDH technique and use the error signal to control the radio-frequency (rf) signal driving the AOMs. The two cavities are separated in frequency by approximately $60 \text{ MHz}/\nu_{\text{FSR}}$, with free spectral range $\nu_{\text{FSR}} = c/2L = 3 \text{ GHz}$, cavity length $L = 50 \text{ mm}$, and speed of light c .

During the experiments, we actively stabilize the intensity of the laser beams coupled to the cavity. For this stabilization, we split off approximately 1% of the power of each beam and send it onto a photodiode. The photodiode signal is compared to a dc signal to create an error signal, which is then fed into a proportional-integral (PI) controller that actively controls the amplitude of the rf signals of the double-pass AOMs. With this locking scheme, we control the intensity sent to the cavities. The input cavity beams can also be shut off rapidly by turning off the rf power. Disabling the frequency and intensity locks of the two cavity beams does not affect the frequency stability of the Ti:sapphire laser, since its frequency is prestabilized.

To characterize the laser noise, we measure the RIN of the laser under three different conditions: (1) when the laser frequency is locked only to the prestabilization cavity, (2)

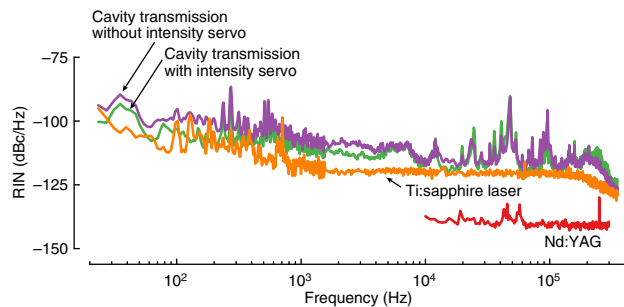


FIG. 8. The characterization of laser noise. The RIN of the Ti:sapphire laser (orange), the transmission of cavity 2 with (green) and without (purple) the intensity servo, compared with the RIN of a low-noise Nd:YAG laser (red).

as in (1) but with additional frequency stabilization to the crossed cavities, and (3) the same as (2) but with intensity stabilization, where conditions (2) and (3) are measured after the transmission through the crossed cavity. In Fig. 8, we show such measurements for cavity 2. For comparison, we also measure the RIN of a commercial low-noise Nd:YAG laser. We use these measurements to estimate the ground-band lifetimes at different trap frequencies in Sec. V.

Finally, an optical heterodyne beat of the Ti:sapphire laser and the optical-frequency comb is used to monitor the absolute frequency of the laser. By simultaneously measuring this frequency and the frequency of the double-pass AOMs that are used for locking, we can determine the absolute frequencies of both cavity modes used to trap the atoms. We use this method to measure the long-term stability of our experimental setup in Sec. VI.

2. Optical transport

The transport beam propagates along the x axis as shown in Fig. 2(c), has a $1/e^2$ beam waist of $50 \mu\text{m}$, and induces a trap depth of $k_B \times 45 \mu\text{K}$, where k_B is the Boltzmann constant. During transport, atoms spread axially over a few millimeters due to the weak axial confinement of the transport beam and the temperature of the atomic cloud rises to approximately $7 \mu\text{K}$.

3. Clock excitation

In our experiments, the clock-excitation dynamics are susceptible to decoherence mechanisms due to elastic e - g collisions and fast inelastic e - e collisions in ^{88}Sr [52]. The elastic collisions reset the coherence between g and e while the population stays constant, while inelastic collisions cause atom loss.

To distinguish between the two effects, we use a detection scheme that can image both g and e atoms separately. To image the in-trap density of g atoms, we use absorption imaging on the 1S_0 - 1P_1 transition [45] as explained in the main text. To image e atoms, we remove g atoms

by applying light resonant with the 1S_0 - 1P_1 transition and repump e back to g by applying 679-nm and 707-nm laser light resonant with the 3P_0 - 3S_1 and 3P_2 - 3S_1 transitions, respectively [52].

Using the above method, we excite atoms in the center of the lattices and take g and e images at different clock-excitation durations. From these measurements, we study how the total atom number, i.e., $N_g + N_e$, and the excited-state fraction, i.e., $N_e/(N_g + N_e)$, evolve as a function of the clock-excitation duration, where N_s specifies the number of atoms in state s . Since we work with non-magic lattices and an imaging resolution of $5.40(8) \mu\text{m}$, the excited-state fraction derived from each pixel is averaged over many different clock-laser detunings. For this reason, we study the clock-excitation dynamics at the center of the lattices, where the lattice envelope is flattest. The results obtained from averaging the central four pixels are plotted in Fig. 9, where we repeat the measurement at two different magnetic fields, 45 G and 225 G, respectively. Following Ref. [51], the different magnetic field values proportionally scale the Rabi frequency Ω [51]. Therefore, we are rescaling the clock-laser duration according to the strength of the magnetic field.

We observe a decay of the total number of atoms as shown in the bottom of Fig. 9, which is expected due to the inelastic e - e collisions [52]. At the center of the atomic cloud, we estimate approximately 1 atom per lattice site on average from the *in situ* images. Assuming a Poisson distribution, we expect that approximately 40% of the populated lattice sites are occupied by more than one atom. Therefore, the clock spectroscopy in our setup is susceptible to atom loss. Here, this loss is advantageous in characterizing the potential, because it enhances the signal-to-noise ratio

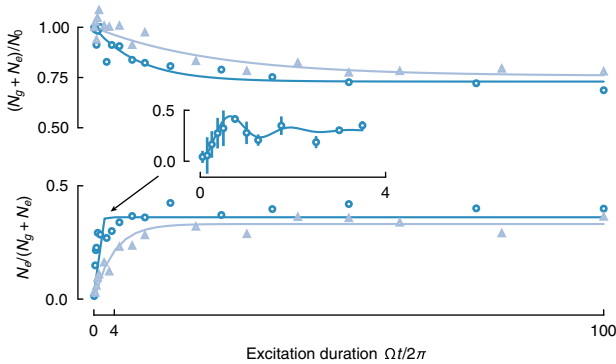


FIG. 9. The clock-excitation dynamics. The total atom number $N_g + N_e$ normalized to the initial total atom number N_0 (top) and the excited fraction (bottom) as a function of the clock-excitation duration. The inset is an enlarged portion of the initial excitation dynamics, fitted with an exponentially decaying sine. The measurements are repeated with an external magnetic field at approximately 45 G (triangles) and approximately 225 G (circles). The data are fitted with exponential functions as a guide to the eye.

of the ground-state depletion images used for the technique. From the data shown in Fig. 9, we expect that the 40% of the atoms lost from the trap and 60% of the e atoms create the depleted images used in Sec. III.

From the dynamics of the excited-state fractions shown in Fig. 9 (top), we observe an exponential rise to a steady-state value, which resembles strongly dephased Rabi dynamics. At a high magnetic field of 225 G, at which we expect $\Omega \sim 2\pi \times 500$ Hz, we observe clear Rabi oscillations that quickly dephase as shown in the inset of Fig. 9 (top). In addition to elastic collisions, there are several other mechanisms that can cause dephasing in our experiments, such as misalignment of the clock probe beam [54], the clock-laser line width, the clock and lattice laser-intensity noise, and the effect of averaging several pixels where each pixel contains contributions from many clock-laser detunings. Among these possibilities, our estimates show that the lattice-intensity fluctuations are the most dominant dephasing mechanism. At a differential ac Stark shift of approximately 400 kHz, a fractional lattice-intensity stability of approximately 10^{-3} causes inhomogeneity in δ of 400 Hz, which is already on the order of $\Omega/2\pi$ at 225 G. Our setup is particularly susceptible to lattice-intensity noise because the techniques described in the main text rely on a large differential ac Stark shift. Such susceptibility to the lattice-intensity noise can be removed by creating the lattices at the magic wavelength.

APPENDIX B: MOTT-INSULATOR SIZE ESTIMATE

One of the most common initial states for quantum simulations is a Mott insulator, a low-entropy initial state in which a single atom occupies each lattice site. Since this is the starting state, the achievable Mott-insulator size determines the size and thus the complexity of the simulation. In this appendix, we show how this Mott-insulator size depends on the waists of the beams that create the optical lattices.

The most important energy scales of quantum simulation in optical lattices are t and U , which, respectively, characterize the tunneling rate of atoms between neighboring sites and the interaction energy between two atoms on the same site as shown in Fig. 10(a). In two dimensions, a fermionic spin-1/2 Mott insulator forms when the interaction energy U is approximately the same as the ground bandwidth $8t$ [11], filling each lattice site with exactly one atom.

However, since the lattice is not perfectly flat, there is an additional site-specific energy offset ΔE as shown in Fig. 10(b). This offset leads to an additional constraint, $\Delta E < U$, which limits the size of the Mott insulator. To estimate the system size, we first estimate at which lattice depth the constraint $U = 8t$ is satisfied [11]. Following Ref. [20],

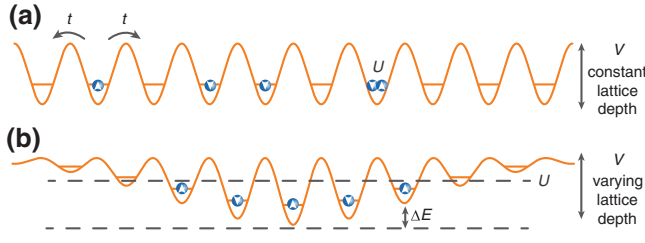


FIG. 10. Fermionic atoms in an optical lattice. (a) Ultracold fermionic atoms trapped in infinitely extended optical lattices of depth V can tunnel between sites at rate t . Two fermions of opposite spin on the same site interact with interaction energy U . (b) Finite-sized optical lattices vary quadratically in depth, causing a site-dependent energy offset ΔE , typically referred to as harmonic confinement or a lattice envelope.

$$U = \sqrt{8/\pi} ka E_{\text{rec}} (V/E_{\text{rec}})^{3/4}, \quad (\text{B1})$$

$$t \sim \frac{4}{\sqrt{\pi}} E_{\text{rec}} \left(\frac{V}{E_{\text{rec}}} \right)^{3/4} \exp \left[-2 \left(\frac{V}{E_{\text{rec}}} \right)^{1/2} \right], \quad (\text{B2})$$

where $k = 2\pi/\lambda$ and a are the wave vector and the scattering length, respectively. The lattice potential can be approximated as

$$V(x_1, x_2) \sim V [e^{-2x_1^2/w^2} \cos^2(kx_1) + e^{-2x_2^2/w^2} \cos^2(kx_2)]. \quad (\text{B3})$$

Using the above expressions, a Mott insulator forms when $V = E_{\text{rec}} [\ln(8\sqrt{2}/ka)]^2/4$. Let us consider the fermionic isotope ^{87}Sr , which has $a = 96a_0$, where a_0 is the Bohr radius, and a nuclear spin $I = 9/2$. When using nuclear-spin-polarized atoms in a mixture of $|g, m_I = \pm 9/2\rangle$ in optical lattices created at a wavelength of 914 nm, the transition to a Mott insulator is expected to occur at $V \sim 8E_{\text{rec}}$. At this depth, the interaction energy U is approximately 728 Hz. We can compare this energy U with the site-specific ΔE to estimate the size of the Mott insulator. The site-specific energy ΔE scales with the harmonic confinement of the lattice, $M\omega^2 r^2/2$, where $r^2 = x_1^2 + x_2^2$ and $\omega = \sqrt{4V/Mw^2}$ is the radial trap frequency. Here, M is the mass of a ^{87}Sr atom and w is the $1/e^2$ waist of the beams that create the lattices.

Setting $\Delta E = U$, we find the radius of the Mott insulator, $r_{\text{Mott}} = w\sqrt{U/2V}$. Considering the waist of our cavity modes $w = 489(8) \mu\text{m}$, we expect a radius of approximately $60 \mu\text{m}$. The area defined by this radius corresponds to the region where the lattice depth is within 96–97% of the maximum. The total atom number in this region $N_{\text{atoms}} = \pi r^2/(\lambda/2)^2$ which is 4×10^4 to 11×10^4 depending on the wavelength, which ranges from 1064 to 689 nm. Performing the same estimates with a waist of $80 \mu\text{m}$, as used in Ref. [57], we obtain an atom number ranging from 1×10^3 to 3×10^3 for the same wavelength range.

APPENDIX C: FITTING-FUNCTION DERIVATION

In this appendix, we derive the fitting function used in Sec. III, describing the spatially dependent detuning that is resonant with the clock transition.

The energy shift of each clock state can be decomposed into two parts: a shift induced by the ac Stark effect and the zero-point vibrational energy in each lattice site. The former is given by $-\alpha_k I(x_1, x_2)/2\epsilon_0 c$, where ϵ_0 is the vacuum permittivity, $I(x_1, x_2)$ is the total lattice intensity from both lattices, and k labels the state e or g . In orthogonal 2D optical lattices where the two lattices have an identical beam waist w , we can write the lattice envelope as $I(x_1, x_2) = I_0 [e^{-2(x_1-x_1^0)^2/w^2} + (1+\epsilon)e^{-2(x_2-x_2^0)^2/w^2}]$, where ϵ specifies the intensity balance between the two lattices, I_0 is the peak intensity, and x_j^0 specifies the position of the lattice-intensity maximum. The second cause of the energy shift is the zero-point vibrational energy of each state. Assuming that the atoms occupy the vibrational ground state, the zero-point energy experienced by each state is given by $\hbar\nu_t^k(x_j)/2$ per lattice axis, where $\nu_t^k(x_j)$ specifies the on-site lattice trap frequency that state k experiences along the lattice axis x_j . The lattice trap frequency also depends on the polarizability and the light intensity. Following the above definitions, $\nu_t^k(x_1) = 2\sqrt{\nu_{\text{rec}}\alpha_k I(x_1)/(2c\epsilon_0\hbar)}$ and $\nu_t^k(x_2) = 2\sqrt{\nu_{\text{rec}}(1+\epsilon)\alpha_k I(x_2)/(2c\epsilon_0\hbar)}$.

The resonant condition occurs when the detuning with respect to the free-space resonance matches the additional shifts,

$$\begin{aligned} \delta_{\text{res}} = & \frac{1}{2\epsilon_0 c \hbar} (\alpha_g - \alpha_e) I(x_1, x_2) \\ & + \sqrt{\frac{\nu_{\text{rec}} I(x_1)}{2c\epsilon_0 \hbar}} (\sqrt{\alpha_e} - \sqrt{\alpha_g}) \\ & + \sqrt{\frac{\nu_{\text{rec}} (1+\epsilon) I(x_2)}{2c\epsilon_0 \hbar}} (\sqrt{\alpha_e} - \sqrt{\alpha_g}). \end{aligned} \quad (\text{C1})$$

In our experiments, we spectroscopically measure the peak trap frequency of g or e to calibrate the peak lattice intensity I_0 and the polarizability ratio α_g/α_e . We rewrite the above expression with respect to these quantities, where the peak trap frequency is $\nu_t^k = 2\sqrt{\nu_{\text{rec}}\alpha_k I_0/(2c\epsilon_0\hbar)}$. Then, we can rewrite δ_{res} as

$$\begin{aligned} \delta_{\text{res}} = & \frac{1}{\nu_{\text{rec}}} \left(\frac{\nu_t^e}{2} \right)^2 \left(\frac{\alpha_g}{\alpha_e} - 1 \right) \\ & \times \left[e^{-2(x_1-x_1^0)^2/w^2} + (1+\epsilon)e^{-2(x_2-x_2^0)^2/w^2} \right] \\ & + \frac{\nu_t^e (e^{-(x_1-x_1^0)^2/w^2})}{2} \left(1 - \sqrt{\frac{\alpha_g}{\alpha_e}} \right) \\ & + \frac{\nu_t^e \sqrt{1+\epsilon} (e^{-(x_2-x_2^0)^2/w^2})}{2} \left(1 - \sqrt{\frac{\alpha_g}{\alpha_e}} \right), \end{aligned} \quad (\text{C2})$$

where we choose the excited-state trap frequency ν_i^e rather than the ground-state trap frequency for convenience.

We fit the data described in Sec. III to the fitting function shown in Eq. (C2) with an additional frequency offset f_0 . The fitted parameters are x_1^0, x_2^0, f_0, w , and ε . We obtain a cavity-mode waist of 489(8) μm with a reduced χ^2 of approximately 5, as discussed in the main text.

APPENDIX D: POTENTIAL SOURCES OF RESIDUAL FRINGES

The presence of the fringes in Fig. 4(d) in the main text is surprising, since the mode-cleaning effect of the cavities is expected to lead to a clean potential. We consider three possible scenarios in which the light circulating within the cavities can exhibit such fringes: (1) scattering from defects or dust particles on the cavity mirrors, or contributions of higher transverse modes due to (2) mode mixing from imperfect cavity-mirror surfaces, or (3) imperfect input coupling [42].

Based on the fringe wavelengths that we observe, we conclude that a dust particle or scattering center would have to be present at a location displaced approximately 350 μm from the center of the mirror. However, our estimates show that such a scattering center would have to scatter tens of percent of the circulating power into a solid angle of 2π to explain the fringe amplitude that we observe. Given that the fringe amplitude differs by an order of magnitude between each cavity, scattering such a large amount of light should result in a very different finesse for the two cavities. Our *in situ* measurements show that the finesse of both cavities agrees within 10%.

If we associate the fringes with a contribution of other transverse modes, the observed 65- μm fringe spacing requires admixture of $\text{TEM}_{m,m}$ modes with $m > 100$, where m counts the number of nodes in the lattice plane. The beam profile associated with such a mode would have a much larger rms diameter than the 489- μm waist of the TEM_{00} mode that we observe. The mirror profile at such large transverse extents is no longer spherical, because it enters the transition into the flat annulus used for optical contacting [41,42], which might explain the irregular fringe patterns in Fig. 4(d). However, we observe fringes with a peak-to-peak amplitude at the 1% level on top of the expected TEM_{00} profile. This amplitude can only be explained if the cavity enhances the higher-order mode and produces a stable interference pattern between both fundamental and high-order mode. In particular, it is highly improbable that the fringes could be explained by interference between the 40-MHz modulation sidebands used to stabilize the laser to the cavity, because any such interference pattern averages out on the time scales relevant for the atomic motion. An explanation that might be consistent with our observations is an accidental mode degeneracy of the fundamental with a very high-order transverse mode,

such that interference between both modes enhances the fringe contrast.

APPENDIX E: CLOCK STATE POLARIZABILITIES

The polarizability of an electronic state is determined by contributions from the core and valence electrons. The core part of the polarizability can be calculated in the single-electron approximation, including random-phase-approximation corrections [80]. The valence part of the atomic state i is given by the sum of contributions over all electric-dipole-coupled states k . This part can be decomposed further into scalar, vector, and tensor parts. For the clock states of ^{88}Sr , where both states have $J = 0$, only the scalar part contributes [44] and the polarizability can be calculated according to [81]

$$\alpha_k = \frac{2}{3\hbar} \sum_l \frac{\omega_{kl}}{\omega_{kl}^2 - \omega^2} |\langle l|D|k \rangle|^2. \quad (\text{E1})$$

Here, $\langle l|D|k \rangle$ is the reduced dipole matrix element between the clock state k and state l . We use ω_{kl} to denote the corresponding transition frequency. The valence part also

TABLE I. The contributions to the scalar polarizability α_k of the g (e) clock state $5s^2 \ ^1S_0$ ($5s5p \ ^3P_0$) at 914.332 nm. The transition energies ΔE [82] are listed in cm^{-1} and the reduced electric dipole matrix elements $\langle l|D|k \rangle$ and the polarizability contributions [83,84] are shown in atomic units, where e (a_0) is the electron charge (Bohr radius). Here, ‘‘Other’’ refers to contributions from states that are not listed explicitly and ‘‘Core’’ refers to the core polarizability. The uncertainties for individual polarizability contributions result from propagating uncertainties in the matrix elements [84] and lead to the quoted uncertainty for the total polarizability.

State l	ΔE (cm^{-1})	$\langle l D k \rangle$ (ea_0)	α_k ($4\pi\epsilon_0 a_0^3$)
$k = 5s^2 \ ^1S_0$			
$5s5p \ ^3P_1$	14 504	0.1510	0.53
$5s5p \ ^1P_1$	21 698	5.248	248.98
$5s6p \ ^3P_1$	33 868	0.034	0.01
$5s6p \ ^1P_1$	34 098	0.282	0.38
Other			5.8
Core			5.3
Total			261.0 ± 1.2
$k = 5s5p \ ^3P_0$			
$5s4d \ ^3D_1$	3842	2.671	-38.25
$5s6s \ ^3S_1$	14 721	1.968	85.92
$5s5d \ ^3D_1$	20 689	2.450	58.91
$5p^2 \ ^3P_1$	21 083	2.605	64.44
$5s7s \ ^3S_1$	23 107	0.515	2.16
Other			42.07
Core			5.55
Total			220.8 ± 2.3

depends on the frequency ω of the light field interacting with the atom.

We calculate the polarizability of the g (e) clock state $5s^2\ ^1S_0$ ($5s5p\ ^3P_0$) at 914.332 nm in Table I. From the total polarizabilities, we extract $\alpha_g/\alpha_e = 1.18 \pm 0.01$.

-
- [1] A. Ashkin, Optical trapping and manipulation of neutral particles using lasers, *Proc. Natl. Acad. Sci. USA* **94**, 4853 (1997).
- [2] R. Grimm, M. Weidemüller, and Y. B. Ovchinnikov, Optical dipole traps for neutral atoms, *Adv. At. Mol. Opt. Phys.* **42**, 95 (2000).
- [3] C. Gross and I. Bloch, Quantum simulations with ultracold atoms in optical lattices, *Science* **357**, 995 (2017).
- [4] M. Saffman, T. G. Walker, and K. Mølmer, Quantum information with Rydberg atoms, *Rev. Mod. Phys.* **82**, 2313 (2010).
- [5] D. S. Weiss and M. Saffman, Quantum computing with neutral atoms, *Phys. Today* **70**, 44 (2017).
- [6] A. Browaeys and T. Lahaye, Many-body physics with individually controlled Rydberg atoms, *Nat. Phys.* **16**, 132 (2020).
- [7] M. Morgado and S. Whitlock, Quantum simulation and computing with Rydberg-interacting qubits, *AVS Quantum Sci.* **3**, 023501 (2021).
- [8] A. D. Ludlow, M. M. Boyd, J. Ye, E. Peik, and P. O. Schmidt, Optical atomic clocks, *Rev. Mod. Phys.* **87**, 637 (2015).
- [9] A. D. Cronin, J. Schmiedmayer, and D. E. Pritchard, Optics and interferometry with atoms and molecules, *Rev. Mod. Phys.* **81**, 1051 (2009).
- [10] I. M. Georgescu, S. Ashhab, and F. Nori, Quantum simulation, *Rev. Mod. Phys.* **86**, 153 (2014).
- [11] T. Esslinger, Fermi-Hubbard physics with atoms in an optical lattice, *Annu. Rev. Condens. Matter Phys.* **1**, 129 (2010).
- [12] I. de Vega, D. Porras, and J. I. Cirac, Matter-Wave Emission in Optical Lattices: Single Particle and Collective Effects, *Phys. Rev. Lett.* **101**, 260404 (2008).
- [13] A. González-Tudela and J. I. Cirac, Non-Markovian quantum optics with three-dimensional state-dependent optical lattices, *Quantum* **2**, 97 (2018).
- [14] L. Krinner, M. Stewart, A. Pazmiño, J. Kwon, and D. Schneble, Spontaneous emission of matter waves from a tunable open quantum system, *Nature* **559**, 589 (2018).
- [15] J. Argüello-Luengo, A. González-Tudela, T. Shi, P. Zoller, and J. I. Cirac, Analogue quantum chemistry simulation, *Nature* **574**, 215 (2019).
- [16] E. Zohar, J. I. Cirac, and B. Reznik, Quantum simulations of lattice gauge theories using ultracold atoms in optical lattices, *Rep. Prog. Phys.* **79**, 014401 (2015).
- [17] M. Aidelsburger, *et al.*, Cold atoms meet lattice gauge theory, *Phil. Trans. R. Soc. A* **380**, 20210064 (2021).
- [18] E. Oelker, R. B. Hutson, C. J. Kennedy, L. Sonderhouse, T. Bothwell, A. Goban, D. Kedar, C. Sanner, J. M. Robinson, G. E. Marti, D. G. Matei, T. Legero, M. Giunta, R. Holzwarth, F. Riehle, U. Sterr, and J. Ye, Demonstration of 4.8×10^{-17} stability at 1 s for two independent optical clocks, *Nat. Photon.* **13**, 714 (2019).
- [19] T. Bothwell, C. J. Kennedy, A. Aeppli, D. Kedar, J. M. Robinson, E. Oelker, A. Staron, and J. Ye, Resolving the gravitational redshift across a millimetre-scale atomic sample, *Nature* **602**, 420 (2022).
- [20] I. Bloch, J. Dalibard, and W. Zwerger, Many-body physics with ultracold gases, *Rev. Mod. Phys.* **80**, 885 (2008).
- [21] G. K. Campbell, M. M. Boyd, J. W. Thomsen, M. J. Martin, S. Blatt, M. D. Swallows, T. L. Nicholson, T. Fortier, C. W. Oates, S. A. Diddams, N. D. Lemke, P. Naidon, P. Julienne, J. Ye, and A. D. Ludlow, Probing interactions between ultracold fermions, *Science* **324**, 360 (2009).
- [22] N. D. Lemke, J. von Stecher, J. A. Sherman, A. M. Rey, C. W. Oates, and A. D. Ludlow, p -Wave Cold Collisions in an Optical Lattice Clock, *Phys. Rev. Lett.* **107**, 103902 (2011).
- [23] M. J. Martin, M. Bishof, M. D. Swallows, X. Zhang, C. Benko, J. von Stecher, A. V. Gorshkov, A. M. Rey, and J. Ye, A quantum many-body spin system in an optical lattice clock, *Science* **341**, 632 (2013).
- [24] M. D. Swallows, M. Bishof, Y. Lin, S. Blatt, M. J. Martin, A. M. Rey, and J. Ye, Suppression of collisional shifts in a strongly interacting lattice clock, *Science* **331**, 1043 (2011).
- [25] T. Akatsuka, M. Takamoto, and H. Katori, Three-dimensional optical lattice clock with bosonic ^{88}Sr atoms, *Phys. Rev. A* **81**, 023402 (2010).
- [26] S. L. Campbell, R. B. Hutson, G. E. Marti, A. Goban, N. D. Oppong, R. L. McNally, L. Sonderhouse, J. M. Robinson, W. Zhang, B. J. Bloom, and J. Ye, A Fermi-degenerate three-dimensional optical lattice clock, *Science* **358**, 90 (2017).
- [27] T. L. Nicholson, M. J. Martin, J. R. Williams, B. J. Bloom, M. Bishof, M. D. Swallows, S. L. Campbell, and J. Ye, Comparison of Two Independent Sr Optical Clocks with 1×10^{-17} Stability at 10^3 s, *Phys. Rev. Lett.* **109**, 230801 (2012).
- [28] R. A. Hart, P. M. Duarte, T.-L. Yang, X. Liu, T. Paiva, E. Khatami, R. T. Scalettar, N. Trivedi, D. A. Huse, and R. G. Hulet, Observation of antiferromagnetic correlations in the Hubbard model with ultracold atoms, *Nature* **519**, 211 (2015).
- [29] A. Mazurenko, C. S. Chiu, G. Ji, M. F. Parsons, M. Kanász-Nagy, R. Schmidt, F. Grusdt, E. Demler, D. Greif, and M. Greiner, A cold-atom Fermi-Hubbard antiferromagnet, *Nature* **545**, 462 (2017).
- [30] C. S. Chiu, G. Ji, A. Mazurenko, D. Greif, and M. Greiner, Quantum State Engineering of a Hubbard System with Ultracold Fermions, *Phys. Rev. Lett.* **120**, 243201 (2018).
- [31] M. Gall, N. Wurz, J. Samland, C. F. Chan, and M. Köhl, Competing magnetic orders in a bilayer Hubbard model with ultracold atoms, *Nature* **589**, 40 (2021).
- [32] D. Wei, A. Rubio-Abadal, B. Ye, F. Machado, J. Kemp, K. Srakaew, S. Hollerith, J. Rui, S. Gopalakrishnan, N. Y. Yao, I. Bloch, and J. Zeiher, Quantum gas microscopy of Kardar-Parisi-Zhang superdiffusion (2021), [ArXiv:2107.00038](https://arxiv.org/abs/2107.00038).
- [33] A. Bruschi, R. Le Targat, X. Baillard, M. Fouché, and P. Lemonde, Hyperpolarizability Effects in a Sr Optical Lattice Clock, *Phys. Rev. Lett.* **96**, 103003 (2006).
- [34] L. Yi, S. Mejri, J. J. McFerran, Y. L. Coq, and S. Bize, Optical Lattice Trapping of ^{199}Hg and Determination of

- the Magic Wavelength for the Ultraviolet $^1S_0 \leftrightarrow ^3P_0$ Clock Transition, *Phys. Rev. Lett.* **106**, 073005 (2011).
- [35] A. P. Kulosa, D. Fim, K. H. Zipfel, S. Rühmann, S. Sauer, N. Jha, K. Gibble, W. Ertmer, E. M. Rasel, M. S. Safronova, U. I. Safronova, and S. G. Porsev, Towards a Mg Lattice Clock: Observation of the $^1S_0 - ^3P_0$ Transition and Determination of the Magic Wavelength, *Phys. Rev. Lett.* **115**, 240801 (2015).
- [36] R. C. Brown, N. B. Phillips, K. Beloy, W. F. McGrew, M. Schioppo, R. J. Fasano, G. Milani, X. Zhang, N. Hinkley, H. Leopardi, T. H. Yoon, D. Nicolodi, T. M. Fortier, and A. D. Ludlow, Hyperpolarizability and Operational Magic Wavelength in an Optical Lattice Clock, *Phys. Rev. Lett.* **119**, 253001 (2017).
- [37] A. Yamaguchi, M. S. Safronova, K. Gibble, and H. Katori, Narrow-Line Cooling and Determination of the Magic Wavelength of Cd, *Phys. Rev. Lett.* **123**, 113201 (2019).
- [38] A. Kawasaki, B. Braverman, E. Pedrozo-Peñafiel, C. Shu, S. Colombo, Z. Li, and V. Vuletić, Trapping ^{171}Yb atoms into a one-dimensional optical lattice with a small waist, *Phys. Rev. A* **102**, 013114 (2020).
- [39] W. Bowden, R. Hobson, I. R. Hill, A. Vianello, M. Schioppo, A. Silva, H. S. Margolis, P. E. G. Baird, and P. Gill, A pyramid MOT with integrated optical cavities as a cold atom platform for an optical lattice clock, *Sci. Rep.* **9**, 11704 (2019).
- [40] Y. Cai, D. G. Allman, J. Evans, P. Sabharwal, and K. C. Wright, Monolithic bowtie cavity traps for ultracold gases, *J. Opt. Soc. Am. B* **37**, 3596 (2020).
- [41] A. Heinz, Ultracold strontium in state-dependent optical lattices, Ph.D. thesis, Department of Physics, Ludwig-Maximilians-Universität München (2020).
- [42] A. Heinz, J. Trautmann, N. Šantić, A. J. Park, I. Bloch, and S. Blatt, Crossed optical cavities with large mode diameters, *Opt. Lett.* **46**, 250 (2021).
- [43] A. González-Tudela and J. I. Cirac, Quantum Emitters in Two-Dimensional Structured Reservoirs in the Nonperturbative Regime, *Phys. Rev. Lett.* **119**, 143602 (2017).
- [44] A. Heinz, A. J. Park, N. Šantić, J. Trautmann, S. G. Porsev, M. S. Safronova, I. Bloch, and S. Blatt, State-Dependent Optical Lattices for the Strontium Optical Qubit, *Phys. Rev. Lett.* **124**, 203201 (2020).
- [45] S. Snigirev, A. J. Park, A. Heinz, I. Bloch, and S. Blatt, Fast and dense magneto-optical traps for strontium, *Phys. Rev. A* **99**, 063421 (2019).
- [46] J. Léonard, M. Lee, A. Morales, T. M. Karg, T. Esslinger, and T. Donner, Optical transport and manipulation of an ultracold atomic cloud using focus-tunable lenses, *N. J. Phys.* **16**, 093028 (2014).
- [47] D. Leibfried, R. Blatt, C. Monroe, and D. Wineland, Quantum dynamics of single trapped ions, *Rev. Mod. Phys.* **75**, 281 (2003).
- [48] T. Ido and H. Katori, Recoil-Free Spectroscopy of Neutral Sr Atoms in the Lamb-Dicke Regime, *Phys. Rev. Lett.* **91**, 053001 (2003).
- [49] M. Boyd, T. Zelevinsky, A. Ludlow, S. Blatt, T. Zanon-Willette, S. Foreman, and J. Ye, Nuclear spin effects in optical lattice clocks, *Phys. Rev. A* **76**, 022510 (2007).
- [50] J. A. Muniz, D. J. Young, J. R. K. Cline, and J. K. Thompson, Cavity-QED measurements of the ^{87}Sr millihertz optical clock transition and determination of its natural linewidth, *Phys. Rev. Res.* **3**, 023152 (2021).
- [51] A. V. Taichenachev, V. I. Yudin, C. W. Oates, C. W. Hoyt, Z. W. Barber, and L. Hollberg, Magnetic Field-Induced Spectroscopy of Forbidden Optical Transitions with Application to Lattice-Based Optical Atomic Clocks, *Phys. Rev. Lett.* **96**, 083001 (2006).
- [52] C. Lisdat, J. S. R. Vellore Winfred, T. Middelmann, F. Riehle, and U. Sterr, Collisional Losses, Decoherence, and Frequency Shifts in Optical Lattice Clocks with Bosons, *Phys. Rev. Lett.* **103**, 090801 (2009).
- [53] M. Bishof, M. Martin, M. Swallows, C. Benko, Y. Lin, G. Quémener, A. Rey, and J. Ye, Inelastic collisions and density-dependent excitation suppression in a ^{87}Sr optical lattice clock, *Phys. Rev. A* **84**, 052716 (2011).
- [54] S. Blatt, J. W. Thomsen, G. K. Campbell, A. D. Ludlow, M. D. Swallows, M. J. Martin, M. M. Boyd, and J. Ye, Rabi spectroscopy and excitation inhomogeneity in a one-dimensional optical lattice clock, *Phys. Rev. A* **80**, 052703 (2009).
- [55] M. McDonald, B. H. McGuyer, G. Z. Iwata, and T. Zelevinsky, Thermometry via Light Shifts in Optical Lattices, *Phys. Rev. Lett.* **114**, 023001 (2015).
- [56] C. Han, M. Zhou, X. Zhang, Q. Gao, Y. Xu, S. Li, S. Zhang, and X. Xu, Carrier thermometry of cold ytterbium atoms in an optical lattice clock, *Sci. Rep.* **8**, 7927 (2018).
- [57] S. Blatt, A. Mazurenko, M. F. Parsons, C. S. Chiu, F. Huber, and M. Greiner, Low-noise optical lattices for ultracold ^6Li , *Phys. Rev. A* **92**, 021402(R) (2015).
- [58] T. A. Savard, K. M. O'Hara, and J. E. Thomas, Laser-noise-induced heating in far-off resonance optical traps, *Phys. Rev. A* **56**, R1095 (1997).
- [59] A. Mosk, S. Jochim, H. Moritz, T. Elsässer, M. Weidemüller, and R. Grimm, Resonator-enhanced optical dipole trap for fermionic lithium atoms, *Opt. Lett.* **26**, 1837 (2001).
- [60] J. Lodewyck, P. G. Westergaard, A. Lecallier, L. Lorini, and P. Lemonde, Frequency stability of optical lattice clocks, *New J. Phys.* **12**, 065026 (2010).
- [61] G. M. Harry, and the LIGO Scientific Collaboration, Advanced LIGO: The next generation of gravitational wave detectors, *Class. Quantum Gravity* **27**, 084006 (2010).
- [62] R. Le Targat, L. Lorini, Y. Le Coq, M. Zawada, J. Guéna, M. Abgrall, M. Gurov, P. Rosenbusch, D. G. Rovera, B. Nagórny, R. Gartman, P. G. Westergaard, M. E. Tobar, M. Lours, G. Santarelli, A. Clairon, S. Bize, P. Laurent, P. Lemonde, and J. Lodewyck, Experimental realization of an optical second with strontium lattice clocks, *Nat. Commun.* **4**, 1 (2013).
- [63] S. Schiller, *et al.*, in *2012 European Frequency and Time Forum* (IEEE, 2012), p. 412.
- [64] T. Nicholson, S. Campbell, R. Hutson, G. Marti, B. Bloom, R. McNally, W. Zhang, M. Barrett, M. Safronova, G. Strouse, W. Tew, and J. Ye, Systematic evaluation of an atomic clock at 2×10^{-18} total uncertainty, *Nat. Commun.* **6**, 6896 (2015).
- [65] P. Lemonde and P. Wolf, Optical lattice clock with atoms confined in a shallow trap, *Phys. Rev. A* **72**, 033409 (2005).
- [66] C. Shi, J.-L. Robyr, U. Eismann, M. Zawada, L. Lorini, R. Le Targat, and J. Lodewyck, Polarizabilities of the ^{87}Sr clock transition, *Phys. Rev. A* **92**, 012516 (2015).

- [67] I. Ushijima, M. Takamoto, M. Das, T. Ohkubo, and H. Katori, Cryogenic optical lattice clocks, *Nat. Photon.* **9**, 185 (2015).
- [68] K.-N. Schymik, S. Pancaldi, F. Nogrette, D. Barredo, J. Paris, A. Browaeys, and T. Lahaye, Single Atoms with 6000-Second Trapping Lifetimes in Optical-Tweezer Arrays at Cryogenic Temperatures, *Phys. Rev. Appl.* **16**, 034013 (2021).
- [69] K. Shibata, R. Yamamoto, Y. Seki, and Y. Takahashi, Optical spectral imaging of a single layer of a quantum gas with an ultranarrow optical transition, *Phys. Rev. A* **89**, 031601(R) (2014).
- [70] G. E. Marti, R. B. Hutson, A. Goban, S. L. Campbell, N. Poli, and J. Ye, Imaging Optical Frequencies with 100 μ Hz Precision and 1.1 μ m Resolution, *Phys. Rev. Lett.* **120**, 103201 (2018).
- [71] A. Daley, M. Boyd, J. Ye, and P. Zoller, Quantum Computing with Alkaline-Earth-Metal Atoms, *Phys. Rev. Lett.* **101**, 170504 (2008).
- [72] A. J. Daley, J. Ye, and P. Zoller, State-dependent lattices for quantum computing with alkaline-earth-metal atoms, *Eur. Phys. J. D* **65**, 207 (2011).
- [73] A. J. Daley, Quantum computing and quantum simulation with group-II atoms, *Quantum Inf. Process.* **10**, 865 (2011).
- [74] A. González-Tudela and J. I. Cirac, Markovian and non-Markovian dynamics of quantum emitters coupled to two-dimensional structured reservoirs, *Phys. Rev. A* **96**, 043811 (2017).
- [75] S. B. Koller, J. Grotti, S. Vogt, A. Al-Masoudi, S. Dörscher, S. Häfner, U. Sterr, and C. Lisdat, Transportable Optical Lattice Clock with 7×10^{-17} Uncertainty, *Phys. Rev. Lett.* **118**, 073601 (2017).
- [76] J. Grotti, *et al.*, Geodesy and metrology with a transportable optical clock, *Nat. Phys.* **14**, 437 (2018).
- [77] P. Wolf, *et al.*, Quantum physics exploring gravity in the outer solar system: The SAGAS project, *Exp. Astron.* **23**, 651 (2009).
- [78] S. Origlia, M. S. Pramod, S. Schiller, Y. Singh, K. Bongs, R. Schwarz, A. Al-Masoudi, S. Dörscher, S. Herbers, S. Häfner, U. Sterr, and C. Lisdat, Towards an optical clock for space: Compact, high-performance optical lattice clock based on bosonic atoms, *Phys. Rev. A* **98**, 053443 (2018).
- [79] Y. Wang, S. Shevate, T. M. Wintermantel, M. Morgado, G. Lothead, and S. Whitlock, Preparation of hundreds of microscopic atomic ensembles in optical tweezer arrays, *npj Quantum Inf.* **6**, 54 (2020).
- [80] M. S. Safronova, W. R. Johnson, and A. Derevianko, Relativistic many-body calculations of energy levels, hyperfine constants, electric-dipole matrix elements, and static polarizabilities for alkali-metal atoms, *Phys. Rev. A* **60**, 4476 (1999).
- [81] M. S. Safronova, Z. Zuhrianda, U. I. Safronova, and C. W. Clark, Extracting transition rates from zero-polarizability spectroscopy, *Phys. Rev. A* **92**, 040501(R) (2015).
- [82] A. Kramida, Yu. Ralchenko, J. Reader, and NIST ASD Team, NIST Atomic Spectra Database (ver. 5.8) [Online]. Available <https://physics.nist.gov/asd> [10/30/2020]. National Institute of Standards and Technology, Gaithersburg, Maryland 2020.
- [83] M. S. Safronova, S. G. Porsev, U. I. Safronova, M. G. Kozlov, and C. W. Clark, Blackbody-radiation shift in the Sr optical atomic clock, *Phys. Rev. A* **87**, 012509 (2013).
- [84] M. S. Safronova (private communication).